ozone layer [A. C. Neuendorffer, *J. Geophys. Res.* **101**, 18807 (1996)], and hence in winter it has poor accuracy over the central Antarctic plateau and reduced accuracy at the edge of Antarctica.
5. J. W. Waters *et al.*, *Geophys. Res. Lett.* **20**, 1219 (1993).
6. J.-P. Pommereau and F. Goutail, *ibid.* **15**, 895 (1988).
7. A. E. Jones *et al.*, *J. Quant. Spectrosc. Radiat. Transfer* **54**, 481 (1995).
8. We compared SAOZ ozone to measurements from the Dobson at Faraday in seasons other than winter to test overall stability, and we examined intercepts of Langley plots during all seasons and over a wide range of ozone amounts to test stability of offset. SAOZ observes ozone in the slant path of sunlight through the atmosphere, related to total vertical amount by an air-mass factor (AMF). When observing the zenith sky, sunlight follows a set of parallel paths before being scattered vertically into the instrument, so there is no unique AMF, merely an average AMF that depends on profiles of ozone and air density. By means of a standard radiative transfer scheme [A. Sarkissian, H. K. Roscoe, D. J. Fish, *ibid.*, p. 471], AMFs have now been calculated for each month of the observations, with the use of a mixture of climatological and measured parameters as input.
9. A. Herber *et al.*, *J. Geophys. Res.* **101**, 3921 (1996).
10. G. M. B. Dobson, D. N. Harrison, J. Lawrence, *Proc. R. Soc. London Ser. A* **122**, 456 (1929).
11. M. R. Schoeberl, M. Luo, J. E. Rosenfield, *J. Geophys. Res.* **100**, 5159 (1995).
12. J. D. Mahlman, J. P. Pinto, L. J. Umscheid, *J. Atmos. Sci.* **51**, 489 (1994).
13. J. E. Rosenfield, P. A. Newman, M. R. Schoeberl, *J. Geophys. Res.* **99**, 16677 (1994).
14. G. L. Manney, R. W. Zurek, A. O'Neill, R. Swinbank, *J. Atmos. Sci.* **51**, 2973 (1994).
15. M. C. Abrams *et al.*, *Geophys. Res. Lett.* **23**, 2341 (1996).
16. S. Crewell *et al.*, *J. Geophys. Res.* **100**, 20839 (1995).
17. J. W. Waters, personal communication.
18. H. Vomel, D. J. Hofmann, S. J. Oltmans, J. M. Harris, *Geophys. Res. Lett.* **22**, 2381 (1995).
19. S. Chubachi, in *Proceedings of the Quadrennial Ozone Symposium*, Halkidiki, Greece, 3 to 7 September 1984, C. S. Zerefos and A. Ghazi, Eds. (Reidel, Dordrecht, Netherlands, 1985), pp. 285–289.
20. S. Chubachi, *J. Geophys. Res.* **102**, 1349 (1997).
21. F. Froidevaux *et al.*, *J. Atmos. Sci.* **51**, 2846 (1994).
22. M. L. Santee *et al.*, *Science* **267**, 849 (1995).
23. G. L. Manney *et al.*, *J. Atmos. Sci.* **52**, 3069 (1995).
24. M. P. Chipperfield *et al.*, *J. Geophys. Res.* **101**, 18861 (1996).
25. K. P. Shine, *Q. J. R. Meteorol. Soc.* **113**, 603 (1987).
26. The upstream advection scheme is based on conservation of second-order moments of tracer distribution during advection [M. J. Prather, *J. Geophys. Res.* **91**, 6671 (1986)]. The advection algorithm is stable, accurate, and highly nondiffusive, making the scheme particularly suited to the preservation of sharp gradients, an important consideration where localized chemical processing on polar stratospheric clouds can cause strong inhomogeneities in tracer distributions.
27. M. P. Chipperfield, D. Carriolle, P. Simon, R. Ramaroson, D. J. Lary, *J. Geophys. Res.* **98**, 7199 (1993).
28. R. Swinbank and A. O'Neill, *Mon. Weather Rev.* **122**, 686 (1994).
29. In this study, the model was initialized by assimilating profiles of ozone taken from the MLS data (version 3) [F. Froidevaux *et al.*, *J. Geophys. Res.* **101**, 10,017 (1996)] and profiles of N_2O taken from the cryogenic limb array etalon spectrometer (CLAES) data (version 7) [A. E. Roche *et al.*, *ibid.*, p. 9679]. The MLS and CLAES instruments are on board the upper-atmosphere research satellite (UARS). UARS follows a precessing, 57° inclined orbit. Both MLS and CLAES view in the limb orthogonal to one side of the satellite. In order to view both hemispheres, UARS performs a yaw maneuver every 36 days, so that MLS and CLAES view along the alternate limb. To assemble a near-global set, data from a diurnal cycle either side of a yaw maneuver was chosen. For this study, MLS ozone from the yaw maneuver that started viewing south on 24 May 1994 was used. Because CLAES ceased to function in 1993, N_2O values from June 1992 were used. Assimilation of these data sets involved binning the data according to their equivalent latitude and potential temperature. Other UARS data could not be used because of internal inconsistency (*24*), so to complete the initial data set, 2D model values were used. The vertical structure of the model was modified until the model N_2O field was identical to the assimilated N_2O field. The full set of chemical fields from the model was then mapped into the 3D domain with the use of equivalent latitude and potential temperature as the transfer coordinates. These coordinates allow chemical fields to follow polar-vortex distortions in a realistic way.
30. K. P. Bowman, *J. Geophys. Res.* **98**, 23013 (1993).
31. A. M. Lee, H. K. Roscoe, M. P. Chipperfield, R. L. deZafra, D. J. Hofmann, in preparation.
32. We thank J. C. Farman for suggesting that a SAOZ be placed at Faraday; D. J. Oldham for persistence during its first year there; C. J. Wright, S. Cuthbertson, D. Haigh, F. P. Hindle, M. P. Chipperfield, J. A. Pyle, and G. L. Manney for efforts at Faraday in subsequent years; J. Squires for help with Langley plots; A. Sarkissian for AMF software; M. P. Chipperfield and J. A. Pyle for SLIMCAT software; G. L. Manney for discussions on MLS data; and J.-P. Pommereau for first drawing our attention to the hint of a midwinter maximum in ozone from the SAOZ at Dumont d'Urville.

10 June 1997; accepted 11 August 1997

Time-Domain Holographic Digital Memory

Xiao A. Shen, An-Dien Nguyen, John W. Perry,* David L. Huestis, Ravinder Kachru†

An optical storage technique based on time-domain holography for the rapid recording and readout of page-formatted digital data is demonstrated. Storage of 356 kilobits of data was achieved at a single spatial location in a rare-earth–doped crystal. The digital data were recorded and accurately retrieved at a peak rate of 300 megabits per second without the use of error-correcting codes. The system's raw bit error rate is about 10^{-7}. This low bit error rate was achieved by a detection scheme for extraction of binary data. These results have implications for dynamic optical memory.

Holographic memories, once considered a storage device of the distant future, have come much closer to reality. Instruments that make use of holographic approaches to data storage have been developed and tested for applications such as the identification of fingerprints (*1*). Use of spatial holography to store page-formatted digital optical data in computer-based applications has also been explored, and the results are promising (*2–4*). The memories are believed to be superior to existing technologies, with key features including ultrahigh storage density, rapid data transfer, short data access times, and exceptional reliability.

Although much progress has been achieved in some key areas of holographic data storage, several major technical impediments remain, restricting its application in a broad area, as was promised initially. The most noticeable obstacle has been the slow recording rate of conventional holographic techniques, which record spatial interference patterns generated by two temporally co-existing laser beams. The recording requires, in addition to laser excitation, subsequent electron diffusion in storage materials, as in the case of photorefractive memory, for example. Such processes limit photorefractive technology to applications that are not input intensive, such as memory that is written only once. Success in developing high-performance input-output (I/O)–intensive holographic memories, such as page-oriented dynamic optical random access memory, will require the development of much higher recording speeds while maintaining high storage densities and low bit error rates, the latter being a benchmark for the quality of stored data.

Time-domain holographic memory has emerged as an excellent candidate for such I/O intensive applications (*5*, *6*). This memory not only has features common to conventional spatial holographic recording, such as high capacity and high degree of parallelism, but also some that are complementary to conventional holography, including fast page recording speed and modest laser power requirement. Recent experiments (*6*) show that an exposure time of several microseconds and a peak laser power of less than 200 mW are sufficient to record a high-resolution binary image with the time-domain technique.

Historically, the time-domain holographic approach evolved from an optical transient phenomenon known as stimulated photon echoes (*7*). It is a time-domain or, equivalently, a spectral-domain version of holographic recording. Like conventional

Molecular Physics Laboratory, SRI International, Menlo Park, CA 94025, USA.

*Permanent address: Department of Computer Science and Mathematics, Carleton College, Northfield, MN 55057, USA.

†To whom correspondence should be addressed. E-mail: kachru@mplvax.sri.com

holography, this technique stores data as holograms by using a reference beam and a data beam. These two beams interfere at a recording medium, causing a change of the optical properties of the medium. Unlike in spatial holography, the reference and data beams appear in the form of short laser pulses and do not overlap temporally. In most recording schemes developed to date, the reference pulse precedes the data pulse by several nanoseconds to several microseconds to provide, in addition to a spatial reference, a temporal reference for the recorded holograms (Fig. 1). The interference generated by these two temporally distinct laser pulses occurs in both spectral and spatial domains, giving rise to four-dimensional holograms (*8*).

The spectral interference of the two pulses is recorded in a storage medium [which is often a rare-earth–doped solid such as $Eu^{3+}:Y_2SiO_5$ or Pr^{3+}:YAG (YAG, yttrium-aluminum-garnet)] by laser excitation. Ions such as Eu^{3+} and Pr^{3+} that are responsible for data recording are resonantly excited by the laser pulses to form population gratings that resemble the Fourier spectra of the pulse pair (Fig. 2). These gratings in a carefully chosen material can persist for several hours to perhaps several days at cryogenic temperatures because the recorded information is actually stored as population modulation of hyperfine levels in the ground state (*6*). Because the grating is a direct result of resonant excitation and requires no secondary process, its formation is instantaneous and requires modest laser power; the data recording is therefore inherently fast and efficient, giving rise to high data transfer rates, fast access times, and short latency. These features are ideal for applications such as a dynamic memory.

Data stored as population gratings are retrieved by illuminating the sample with another laser pulse known as the read pulse (Fig. 2), which reconstructs the object field as in conventional holography. However, unlike in conventional holography, the reconstructed field appears as an emitted laser pulse and is temporally distinct from the read pulse, just as in case of recording. For a given temporal separation τ between the write and data pulses, the reconstructed pulse will occur a time τ after the arrival of the read pulse (Fig. 1) and has spatial features identical to those of the stored data pulse. This delayed radiation is often referred to as photon echoes. Mathematically, the Fourier transforms of the echo and three input pulse electrical fields $\tilde{E}$ are related in the following manner

$$\tilde{E}_e(\nu) \propto \tilde{E}^*_W(\nu)\tilde{E}_D(\nu)\tilde{E}_R(\nu) \qquad (1)$$

where the subscripts e, W, D, and R denote echo, write, data, and read pulses, respectively, and ν denotes the frequency. Because the echo is a replica of the data pulse both spatially and temporally, the peak readout rate (the number of bits per echo) is identical to the peak recording rate (the number of bits per data pulse) in a time-domain digital memory.

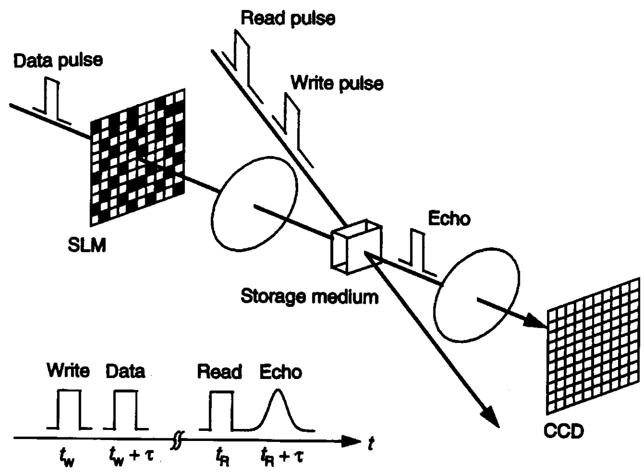

Fig. 1. Time-domain holographic recording scheme. The insert shows the order in which the write, data, read, and reconstructed pulses occur.

The material we chose to demonstrate this recording scheme was crystalline $Eu^{3+}:Y_2SiO_5$ (0.1 atomic %, 7 mm thick). We used its $^7F_0$-$^5D_0$ transition at site 1 (~579.88 nm), which has an inhomogeneously broadened linewidth of ~4 GHz and a dephasing time of ~2 ms (*9*). The product of the two parameters gives the theoretical upper bound for the storage capacity per spatial location as a result of the presence of the wavelength dimension. This material has two optically equivalent sites for the transition; the other site (site 2) has a comparable linewidth and dephasing time (*9*), making the material a good candidate for high-capacity applications. During the experiments, the crystal was kept at a temperature of about 4 K in a flowing He-vapor cryostat.

Digital data pages, each of which contained 3360 bits of data, were generated by illuminating a spatial light modulator (SLM) (*10*) with laser pulses as short as 11.2 μs (*11*), giving rise to a maximum peak (burst) recording rate of 300 megabits per second. Each page was stored in a distinct, narrow (~500 kHz) frequency channel (*12*) within the inhomogeneously broadened absorption line by wavelength-division multiplexing (WDM). The separation between two adjacent channels was chosen to be ~800 kHz. There are distinct advantages to WDM (*13*): (i) Recording and retrieval can be accomplished without the use of any moving parts for laser beam steering, so that it is inherently reliable and often provides short access times (*12*); (ii) there is no significant effect on diffraction efficiency; and (iii) each data page can be recorded in an identical manner, eliminating the need for scheduled or incremental recording, as is used in angular-division multiplexing (*14*).

The retrieved data were captured by an intensified charge-coupled device (CCD) camera and subsequently digitized by a frame grabber (*15*). The SLM and CCD operated at the video rate (30 frames per second, which is the maximum frame rate allowed for the devices), and the resulting digitized data were transferred at the same speed to a computer's dynamic memory. At the present time, the SLM limits the sustainable recording speed to

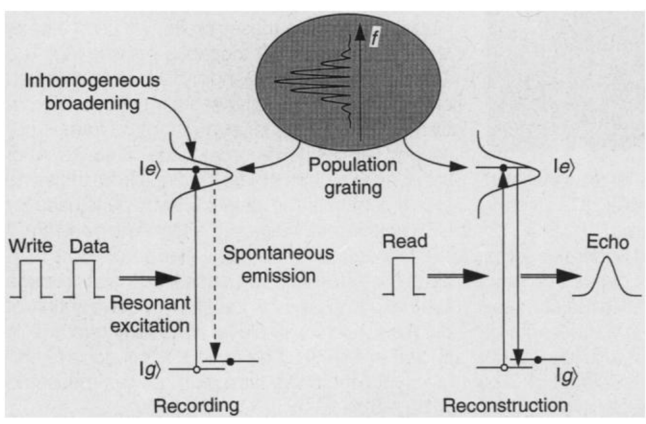

Fig. 2. Schematic of the mechanism for the formation of the population grating and echoes under the laser excitations. Symbols |g⟩ and |e⟩ denote the ground and excited states of an electronic transition, respectively, and the vertical labeled *f* represents the frequency.

~110 kilobits per second, substantially lower than the burst rate of 300 megabits per second permitted by the storage material; however, this limit is not fundamental. High-speed SLMs with a full frame rate of 3 kHz are commercially available; ones with higher speeds are being considered for development. Semiconductor laser arrays may be used in the future to compose binary digital pages without the need of SLMs. Such devices will have a single-channel modulation rate sufficiently high (in excess of 1 GHz) to match the burst rate set by the page exposure time.

In digital memories, one important parameter determining the memory's performance is the bit error rate (BER), which measures how often an error bit occurs on average. This parameter is closely related to other performance parameters of the system, such as storage capacity, data transfer rates, and data access times. In general, for a given system, attempting to reduce the BER leads to a decrease of storage capacity or data transfer rate, or both, because a low BER requires high signal-to-noise ratios, which implies the use of large bit dimensions in the case of parallel recording. For a given frame size, it translates into a decrease of the data transfer rate.

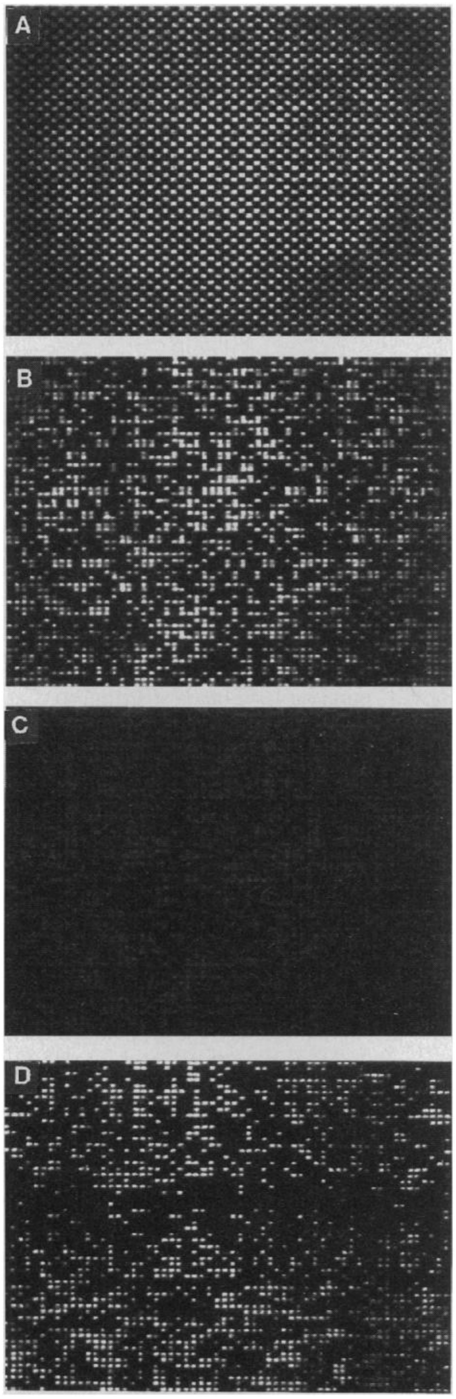

Fig. 3. (**A**) Input data image after transmission through the Eu^{3+}:Y_2SiO_5 sample. (**B**) Reconstructed image after storage in Eu^{3+}:Y_2SiO_5 for 200 μs. (**C**) Image reconstructed under the same conditions as in (B) but with weak overall intensity. (**D**) Image reconstructed 5 min after the completion of recording. In (A) through (C), the length of the data pulse was 11.6 μs, and that in (D) was 50 μs. These times correspond to I/O rates of 300 and 67 megabits per second, respectively.

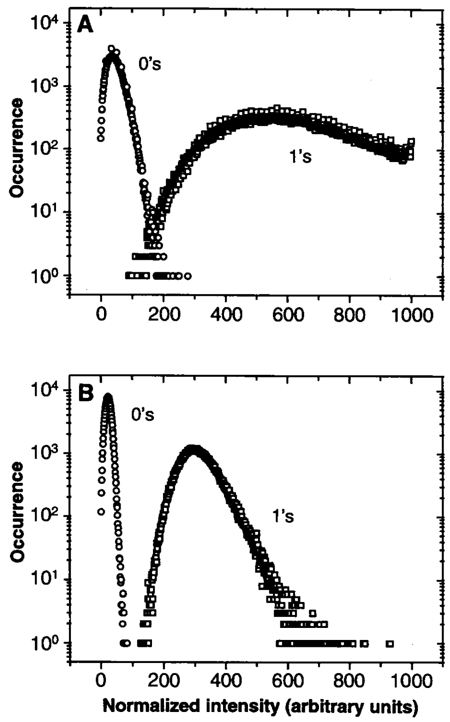

Fig. 4. (**A**) Histogram showing the intensity distributions of 0's and 1's that were retrieved from the time-domain memory. (**B**) Normalized histogram obtained after applying the local threshold technique. In obtaining these results, we used a peak recording rate of 300 megabits per second. The 100 pages were wavelength-division multiplexed at a single storage cell measuring about 1.0 mm by 1.0 mm by 7.0 mm at a rate of 30 frames per second with a total recording time of ~3.3 s. All of the pages used here were obtained from the same experiment. For convenience, each page used for BER analysis was retrieved after being transferred to the memory for 200 μs. The use of short storage time prevented the undesired page-to-page fluctuation caused by the slow frequency drift of our laser. An example of long-term storage is shown in Fig. 3D. The echo (or "diffraction") efficiency for the short-term storage was measured to be $\sim 5 \times 10^{-3}$.

For an optical storage system operating at high I/O speeds with low laser power illumination, the retrieved data are often at a signal level that is limited by shot noise, which is a result of the quantum nature of photons. For page-formatted recording, the process is further complicated by the nonuniform illumination of an SLM. Because of these undesired conditions associated with a low photon budget, such a system often exhibits large page-to-page fluctuations and intrapage variations.

Figure 3A shows a sample input page used in data recording. Spatial variation of the intensity is apparent. This variation reflects the spatial beam mode of the addressing laser, contributing partially to the spatial signal variations within a page discussed earlier. The other contributions include shot noise.

The page-to-page fluctuation is often more noticeable in the retrieved data because it is magnified by less-than-ideal recording and readout conditions. Figure 3, B and C, show two retrieved pages that represent the brightest and dimmest among a total of 100 pages recorded in an experiment. They are single readout events with no signal averaging. The intensity difference between the two pages is >300%, which is mainly caused by the frequency instability of the laser system (*12*).

Examination of the histogram of all 100 pages (totaling 336 kilobits of data) reveals that the intensity distributions of the 1's (or ON's) and 0's (or OFF's) partially overlap (Fig. 4A). If a single threshold were used to determine all of the data bits, it would lead to a BER as large as 10^{-3}, which is not suitable for any storage application.

The broad distribution curves in Fig. 4A are mainly a reflection of the interpage intensity fluctuations and intrapage variations. The broadening also includes cross talk between neighboring 1's and 0's. If these intensity variations and cross talk were removed, the distributions for both 1's and 0's would follow closely scaled Poisson distributions, which has been confirmed experimentally for known images. Under this condition, a single threshold can be obtained for the whole page with knowledge of the average of the intensities of 1's and 0's only. This finding allows us to develop the following scheme to rapidly and accurately read page-formatted binary data that have large intrapage intensity variations and large interpage fluctuations.

We use recently determined data bits to obtain a local threshold for the next bit under consideration. The local region is chosen in such a way that it occupies an area that is small enough so that the illumination is approximately uniform yet large enough to have a sufficient number of bits for an adequate average. Under such a condition, a threshold can be derived from the scaled Poisson distributions to accurately determine the state of the bit, provided that the intensity within a page varies smoothly. We adopted the following formula for the threshold

$$I_{\text{thr}} = I_0 + p\sqrt{I_0} + q[(I_1 - p\sqrt{I_1}) - (I_0 + p\sqrt{I_0})] \quad (2)$$

where I_0 and I_1 are the average intensities of 0's and 1's, q is a weighting factor (chosen empirically to be ⅓), and p is a measure of at how many standard deviations above I_0 and below I_1 we can place the threshold. Here, we use $p = 11$. The optimum numbers used in averaging were found to be 4 for 0's and 8 for 1's.

Initial values of I_0 and I_1 are needed to jump start the analysis of each page. This is accomplished by permanently setting to 0 four known bits at the corners of a 4×4 region in the center of the SLM, where the signal-to-noise rate is largest. We average the 4 bits to estimate I_0. A crude estimate for I_1 can be obtained by averaging the intensities of the remaining 12 unknown bits. The threshold for the block is then calculated from Eq. 2 by assuming the block intensity $I_{\text{block}} = (I_0 + I_1)/2$, which implies an equal number of 1's and 0's in the block. This approach yields a BER of 10^{-6} for the 12-bit central region, or equivalently, a 10^{-5} probability of having an error bit per page.

We then continue this analysis process by spiraling outward from the center of a page toward the edges, with the intensity decreasing gradually as the analysis proceeds. The neighboring 1's and 0's are stored in two separate register arrays and updated in a first-in–first-out manner to obtain their running averages. Thus, each data bit is determined in real time with the use of Eq. 2. In comparison to existing schemes for reading page-formatted digital data (*2, 16*), this automatic threshold calibration technique uses no coding bits and requires no mathematical iteration. These advantages lead to a significant increase in the readout rate, which is ideal for high-speed applications.

Using this approach, we repeated the above experiment and obtained a histogram for the same 100 pages used earlier (Fig. 4B). This histogram was normalized to the respective threshold of each data bit and shows two clearly separate distribution curves. The separation is ~40% of the full width of the distribution for 0's. This large separation suggests an effective increase of the system's dynamic range by ~40%. The raw BER is estimated to be $\sim 10^{-7}$. We further verified this number by repeating the experiment 10 times: The two distribution curves in the resulting histogram remained separate.

According to our BER measurement, our current storage system is capable of recording close to 10 megabits of digital data without generating an error bit. To demonstrate it, we stored a high-resolution black-and-white photograph of Albert Einstein (Fig. 5A). The digitized photograph contains 106 pages, totaling 356 kilobits, of digital data. Figure 5B shows the reconstructed photograph after being copied to and read back from the memory. The entire photograph was stored at a single spatial location in Eu^{3+}:Y_2SiO_5 using WDM with a peak recording speed of 300 megabits per second, and no error correcting code of any kind was used. The total material bandwidth used was only ~85 MHz.

Because Eu^{3+}:Y_2SiO_5 has two equivalent optical sites with a total of ~8 GHz inhomogeneous bandwidth, 85 MHz represents only ~1% of the available storage capacity at this location. In principle, 100 such photographs can be wavelength multiplexed at this spatial location, which implies a total raw capacity of ~4.5 megabytes. Taking into account the active storage volume used, the projected density is $\sim 6 \times 10^8$ bits per cubic centimeter.

The above estimates were based on simple extrapolation of our current experimental results, which were obtained under conditions that were far from optimum (*15*); therefore, these numbers do not represent the fundamental limits of the storage system. The projected capacity can be increased substantially by using, for example, a matched SLM, CCD, and frame grabber (*3*). Furthermore, the use of SLMs with lower insertion loss would also increase the storage density because higher spatial resolution can be achieved with a high-power addressing beam. Currently, SLMs with an insertion loss of <20% are commercially available. With the rapid advance of peripheral devices, such as SLMs and CCD cameras, the achievable storage capacity is likely to be several orders of magnitude greater than what is projected here.

The recording and readout speeds would also be increased by the use of a SLM with lower insertion loss. We estimate that the length of the data pulse can be reduced by a factor of 5 without loss of signal strength by using a SLM with 20% insertion loss. This adjustment would allow an I/O rate of ~1.5 gigabits per second. Furthermore, by using matched SLMs and CCDs, an I/O rate in excess of 10 gigabits per second should be achievable without any penalty in raw BER.

Parallel digital data storage making use of the time-domain approach could be developed into a high-performance page-oriented dynamic optical memory. As the technology for parallel data access becomes more mature, this time-domain holographic approach along with other optical holographic storage techniques (such as photorefractive memory) may fulfill their long-awaited promise for high-speed, high-density data storage. A number of issues still need to be addressed before this

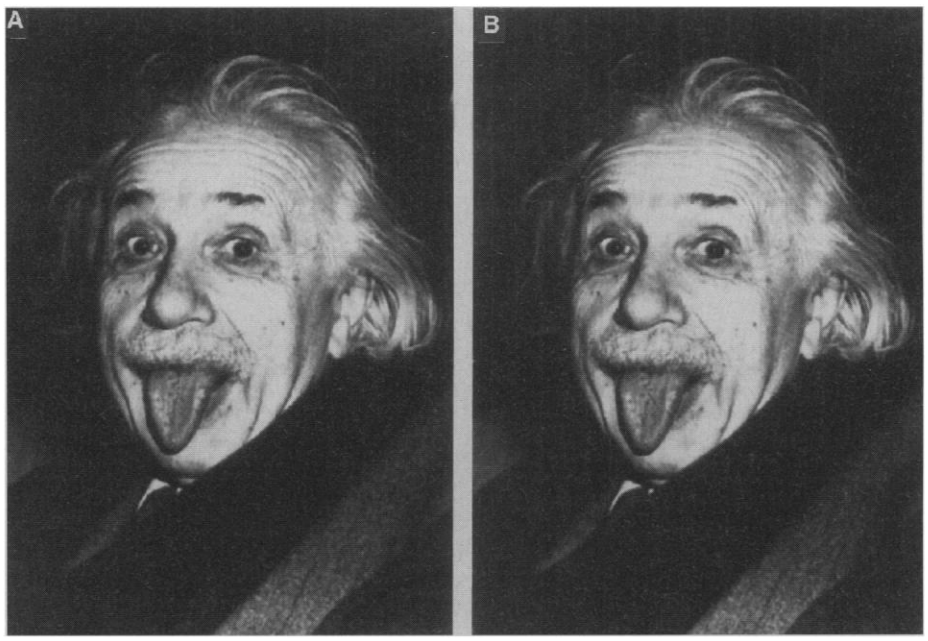

Fig. 5. (**A**) Digitized photograph displayed using its original binary data. (**B**) Same photograph obtained after the binary data was transferred to and then recalled back from the time-domain memory. [Reprinted with permission from UPI/Corbis-Bettman]

technology can be considered commercially viable, such as the low operating temperature currently used, which will require further efforts in the development of high-temperature storage materials.

REFERENCES AND NOTES

1. D. Psaltis and F. Mok, *Sci. Am.* **273**, 70 (November 1995).
2. J. F. Heanue, M. C. Bashaw, L. Hesselink, *Science* **265**, 749 (1994).
3. M. P. Bernal *et al.*, *MRS Bull.* **21**, 51 (1996).
4. E. S. Maniloff *et al.*, *Appl. Opt.* **34**, 4140 (1995).
5. T. W. Mossberg, *Opt. Lett.* **7**, 77 (1982).
6. X. A. Shen, E. Chiang, R. Kachru, *ibid.* **19**, 1246 (1994).
7. T. Mossberg, R. Kachru, S. R. Hartmann, A. Flusberg, *Phys. Rev. A* **20**, 1976 (1979); V. V. Samartsev, R. G. Usmanov, G. M. Ershov, B. Sh. Khamidullin, *Sov. Phys. JETP* **47**, 1030 (1978); V. A. Zuikov, V. V. Samartsev, R. G. Usmanov, *JETP Lett.* **32**, 270 (1980); J. B. W. Morsink, W. H. Hesselink, D. A. Wiersma, *Chem. Phys. Lett.* **64**, 1 (1979).
8. The fundamental difference between the present technique and the persistent spectral hole-burning (PSHB) holographic recording [see, for example, A. Renn *et al.*, *J. Lumin.* **38**, 37 (1987)] is that in PSHB, the sample is exposed simultaneously to two laser beams and a spectral hole is burned at the laser wavelength. The depth of the hole at a given spatial location varies according to the spatial interference pattern generated by both beams, and no temporal information is recorded in the holograms. These holograms are known as volume holograms, identical to those obtained in photorefractive memories. The technique also differs significantly from the accumulated photon echo (APE) memory in that APE uses multiple pairs of write and data pulses to record a single image at one spectral location [P. Saari, R. Kaarli, A. Rebane, *J. Opt. Soc. Am. B* **3**, 527 (1986)].
9. R. Yano, M. Mitsunaga, N. Uesugi, *Opt. Lett.* **16**, 1884 (1991).
10. The SLM used in the present experiment is a liquid-crystal array taken from a commercial projection television. The array consists of 480 pixels by 440 pixels and has a fill factor of ~24%. This low fill factor introduces a large insertion loss in the transmitted beam. We measured the loss for the zeroth-order transmission to be ~97% at 580 nm. We chose a 5×5 region of the SLM to represent a data bit and used a total of 3360 bits (60 bits by 56 bits) in each data frame to cover a center area equal to about 40% (~1.6 cm × 1.3 cm) of the SLM.
11. The length of the data pulse varied from 11.2 to 50 μs. This pulse was biphase-modulated with pseudorandom code [Y. S. Bai and R. Kachru, *Opt. Lett.* **18**, 1189 (1993)] to reduce coherent saturation as well as echo fluctuations caused by laser wavelength instability. The write and read pulses were 10-μs-long square pulses with a peak power of only ~200 mW. These pulses were also biphase-encoded but with the 5-bit Barker code [see, for example, M. N. Cohen, in *Principles of Modern Radar*, J. L. Eaves and E. K. Reedy, Eds. (Van Nostrand Reinhold, New York, 1987), p. 465] to increase the data channel width to ~500 kHz. Such an increase of channel width makes the memory system more tolerant to laser wavelength instability and hence reduces the fluctuation of echo intensity.
12. To achieve the required frequency precision, we used a Coherent ring dye laser and further frequency-stabilized the laser by using the Pound-Drever-Hall method [R. W. P. Drever *et al.*, *Appl. Phys. B* **31**, 97 (1983)]. By using an intracavity electro-optic modulator and locking the laser to an external reference cavity, we substantially reduced laser noise with frequencies above ~1 kHz and achieved a laser linewidth with respect to the cavity of ~40 kHz over a time period of 20 ms. We accomplished WDM by tuning the laser externally with an acousto-optic modulator to achieve a channel access time of ~1 μs.
13. For a detailed discussion on the advantages of using WDM in frequency-selective storage materials, see, for example, B. Kohler *et al.*, *Opt. Lett.* **18**, 2144 (1993).
14. D. Psaltis, D. Brady, K. Wagner, *Appl. Opt.* **27**, 1752 (1988).
15. The intensified CCD camera has an array of 768 pixels by 484 pixels. However, the frame grabber digitizes the captured images at a reduced horizontal resolution of 640 pixels per line. The data frame from the SLM is imaged (1:1) onto the CCD array, resulting in an average bit size of 10.7 pixels × 8.4 pixels after digitization. The mismatch between the frame grabber and CCD, and that between the CCD and SLM, as well as the low spatial resolution of the intensifier (~64 line pairs per millimeter), prevented the use of small bit dimensions. We used these mismatched devices because they were readily available and made no attempt to match their dimensions.
16. M. M. Wang *et al.*, *Opt. Lett.* **22**, 558 (1997).

17. This research was supported by the Defense Advanced Research Projects Agency (DARPA) under contract F49620-95-C-0077 and by Air Force Office of Scientific Research (AFOSR) under contract F49620-95-C-0029. Helpful suggestions and discussions with R. Leheny of DARPA and A. Craig of AFOSR are gratefully acknowledged.

27 May 1997; accepted 22 August 1997

Nanotube Nanodevice

Philip G. Collins, A. Zettl,* Hiroshi Bando, Andreas Thess, R. E. Smalley

A scanning tunneling microscope (STM) was used to explore the local electrical characteristics of single-wall carbon nanotubes. As the STM tip was moved along the length of the nanotubes, well-defined positions were found where the transport current changes abruptly from a graphitic-like response to one that is highly nonlinear and asymmetrical, including near-perfect rectification. The observations are consistent with the existence of localized, on-tube nanodevices of a type proposed theoretically.

Carbon nanotubes (*1*) constitute a fascinating new class of materials with a broad range of potential applications. Electronically, nanotubes are expected to behave as ideal one-dimensional (1D) "quantum wires" with either semiconducting or metallic behaviors, depending on geometrical tube parameters (*2–4*). The joining of dissimilar tubes could result in nonlinear junction devices formed from only a handful of carbon atoms. It has been suggested that localized defects, such as pentagon-heptagon pairs, can be the basis of nanoscale nanotube devices (*5–8*). We used an STM to explore the local electrical characteristics of carbon single-wall nanotubes (SWNTs). By moving the STM tip along the length of the nanotubes, we found well-defined positions where the transport current changes abruptly from a graphitic-like response to one that is highly nonlinear and asymmetrical, including near-perfect rectification. The observations are consistent with the existence of localized, on-tube nanodevices of the type that have been explored theoretically. Such device properties, when combined with the high mechanical strength (*9*) and anticipated high thermal conductivity of nanotubes, point toward several future electrical, mechanical, and electromechanical applications, including those on size scales inaccessible by current lithographic methods.

P. G. Collins and A. Zettl, Department of Physics, University of California at Berkeley, and Materials Sciences Division, Lawrence Berkeley National Laboratory, Berkeley, CA 94720, USA.
H. Bando, Physical Science Division, Electrotechnical Laboratory, Tsukuba, Ibaraki 305, Japan.
A. Thess and R. E. Smalley, Center for Nanoscale Science and Technology, and Departments of Chemistry and Physics, Rice University, Houston, TX 77005, USA.

*To whom correspondence should be addressed. E-mail: azettl@physics.berkeley.edu

The SWNTs used in this study were synthesized through a laser-assisted process described previously (*10*). The nanotubes were purified in oxygen at 750°C to remove undesirable amorphous and graphitic material. X-ray and electron diffraction studies on nanotubes from the same preparation batch indicated that a large proportion of the SWNTs thus produced have 1.36 nm diameters and zero chirality (so-called "armchair" tubes); the tube diameters are presumed uniform over micrometer-length scales.

Crystalline "ropes" of close-packed parallel-aligned tubes tend to form with average diameters of 20 nm. Previous fixed, large-contact electrical conductivity measurements on such nanotube ropes have shown a metallic-like behavior at room temperature and activated or localized behavior at low temperatures, as expected from quantum 1D wires (*11–13*).

We prepared samples suitable for STM characterization by pressing the purified SWNT material onto a gold-coated glass substrate, which left behind a thick film or mat of randomly aligned nanotubes. To eliminate extrinsic sources of damage to the SWNTs, we performed no other processing of the surface. The local electronic structure of the nanotubes was determined with a specially constructed STM with in